Nonlocal enrichment of a micromechanical damage model with tensile softening: advantages and limitations

Wencheng Jin[a], Chloé Arson[a,*]

[a]*School of Civil and Environmental Engineering, Georgia Institute of Technology, USA*

Abstract

Upon crack propagation, brittle geomaterials such as concrete and rock exhibit a nonlinear stress/strain behavior, damage induced stiffness anisotropy, loading path dependent strain softening and hardening, unilateral effects due to crack closure and a brittle-ductile transition, which depends on the confining pressure. Challenges in theoretical and numerical modeling include the distinction between tensile and compressive fracture propagation modes, mesh dependency during softening, and lack of convergence when several critical points are expected on the stress/strain curve. To overcome these issues, we formulate a nonlocal micromechanics based anisotropic damage model. A dilute homogenization scheme is adopted for calculating the deformation energy of the Representative Elementary Volume due to the displacement jumps at open and closed micro-cracks. Tension (respectively compression) damage criteria are expressed in terms of non-local equivalent strains defined in terms of positive principal strains (respectively deviatoric strains). Constitutive parameters are calibrated against published experimental data for concrete and shale. We employ the arc-length control method to solve

*Corresponding author
Email address: chloe.arson@ce.gatech.edu (Chloé Arson)

boundary-value problems with the finite element package OOFEM: the algorithm allows capturing softening, snap back and snap through. We simulate the development of the compression damage zone around a cavity under biaxial far field stress conditions and the softening behavior consequent to tensile fracture propagation during a three-point bending test. No mesh dependency is noted during softening as long as micro-cracks do not interact.
Keywords: Continuum Damage Mechanics, Micromechanics, Anisotropic Damage, Nonlocal regularization, Arc length control, Mixed mode fracture propagation

1. Introduction

Understanding the mechanical behavior of quasi-brittle materials, such as concrete and rocks, is crucial in civil and petroleum engineering, for instance to analyze concrete structure failure or model hydraulic fracturing in reservoir rock. Laboratory experiments and field investigations show that the inception, growth and coalescence of micro cracks at the grain scale induce a complex nonlinear behavior at the macro-scale: tensile softening starts at a very low stress compared to the compressive yield stress, the formation of crack families of different orientations results in anisotropic stiffness reduction, crack closure produces unilateral effects, and in compression, a brittle-ductile transition occurs as the confining pressure is increased [1, 2, 3, 4].

At the scale of a Representative Elementary Volume (REV - typically, the laboratory sample scale), Continuum Damage Mechanics (CDM) models are either based on phenomenology or micromechanics [5]. In phenomenological models, damage is an internal state variable defined as a tensor of

second order [6, 7, 8] or fourth order [9, 10], used to represent anisotropic stiffness reduction. The expression of energy potentials in terms of damage is constrained by symmetry and positivity requirements [11, 12]. In order to satisfy thermodynamic consistency conditions, the energy release rate (damage driving force) that is work-conjugate to damage is used to construct damage criteria and damage potentials [13, 14, 15]. The inconvenient of phenomenological models is that the energy potentials are arbitrarily crafted to match observed stress/strain curves. As a result, constitutive relationships depend on material parameters that do not have any specific physical meaning. By contrast, in micromechanics, the material response at the REV scale is derived from matrix-inclusion interaction laws. Crack surface displacement jumps and local stresses are expressed explicitly and upscaled. Depending on whether the interaction among cracks is considered or not, a variety of homogenization techniques can be used, e.g. the dilute scheme [16, 17, 18, 19, 20], the self-consistent method [21, 22, 23], Mori-Tanaka scheme [24, 25, 26]. All of these models depend on the density of each crack family (i.e. each crack orientation). Cracks of a family are assumed to follow the same geometrical evolution laws, which are derived from fracture mechanics [27, 28]. Under usual matrix-interaction assumptions, micro crack coalescence cannot be captured, which makes it impossible to model softening. In addition, most micromechanical approaches require the implementation of sophisticated iterative algorithms at the material point, which induces huge computational costs [29].

From a numerical perspective, simulation results become mesh-dependent when a local softening constitutive model is used to analyze failure. Strain

localization renders the problem mathematically ill-posed [30, 31]. The regularization techniques that are the most widely used to address this issue are differentiation based and integration based nonlocal formulations. Differentiation-based models are enriched with the first or higher-order gradient of state variables or thermodynamic forces, which allows accounting for the variations of variables within a neighborhood around material points [32, 33, 34, 35]. When the gradients of state variables are used in the formulation, additional degrees of freedom need to be implemented for Finite Element Analysis, for instance the third-order stress tensor (conjugate to the gradient of deformation). In integration based nonlocal models, a variable at a point is calculated as a weighted average over a certain neighborhood of that point [36, 37, 38, 39, 40]. The weights that quantify the intensity of the interaction between Gauss points is tabulated, so that each Gauss point interacts with the Gauss points in its neighborhood. The size of the neighborhood is determined by an internal length parameter. Advantages and limitations of the different regularization techniques are discussed in [41]. Another challenge of failure analysis is non-convergence issues encountered at the global iteration level. The classical Newton-Raphson scheme based on loading control only or displacement control only works when only hardening effects are considered. In case of snap back or snap through, more advanced methods, such as line search [42] or arc length control [43, 44] need to be used.

In this paper, we derive the expression of damage energy potentials from micromechanics to formulate and implement a nonlocal anisotropic damage model. Under the assumption of crack non-interaction, the free enthalpy is

obtained by integrating open and closed crack surface displacement jumps in all possible crack orientations within a unit sphere (Section 2). We construct equivalent strains induced by open and closed cracks. Following a phenomenological approach, we formulate two damage criteria and two damage potentials to predict the evolution of crack density. Single element simulations (at the Gauss point) of cyclic uniaxial tension-compression and triaxial compression tests demonstrate the capabilities of the proposed framework. In Section 3, we explain the theory and implementation of the nonlocal model and we describe the arc length control method employed in the resolution agorithm. In Section 4, we calibrate the proposed damage model against published experimental results of triaxial compression tests performed on shale and uniaxial tension tests performed on concrete. We simulate damage development around a circular cavity, with different combinations of horizontal and vertical stress levels. We also simulate a three-point bending test with the calibrated model parameters.

2. Local anisotropic damage model

2.1. Micromechanics-based Gibbs energy

We adopt the expression of the free enthalpy established in [45], for a REV of volume Ω_r and external boundary $\partial\Omega_r$ subjected to a uniform stress $\boldsymbol{\sigma}$. It is assumed that a large number of penny shaped microscopic cracks of various orientations are embedded in an isotropic linear elastic matrix of compliance tensor $\mathbb{S}_0$. Each microscopic crack is characterized by its normal direction $\overrightarrow{n}$ and its radius a, which is at least 100 times smaller than the REV size. Opposite crack faces are noted ω^+ and ω^-, with normal vectors

$\overrightarrow{n}^+$ and $\overrightarrow{n}^-$. The macro strain of a REV that contains a single set of N microcrack oriented in planes normal to $\overrightarrow{n}$ is the sum of the elastic strains of the matrix and the strains due to the normal and shear crack displacement jumps, denoted as $[u_n]$ and $[\overrightarrow{u_t}]$ respectively. Therefore:

$$\boldsymbol{\epsilon} = \mathbb{S}_0 : \boldsymbol{\sigma} + \frac{N}{|\Omega_r|}\int_{\partial\omega^+}[u_n](\overrightarrow{n}\otimes\overrightarrow{n})\mathrm{d}S + \frac{N}{2|\Omega_r|}\int_{\partial\omega^+}([\overrightarrow{u_t}]\otimes\overrightarrow{n} + \overrightarrow{n}\otimes[\overrightarrow{u_t}])\mathrm{d}S \tag{1}$$

Since it is assumed that cracks do not interact, we use a dilute homogenization scheme. The stress that acts on crack faces is a direct projection of the macroscopic stress (i.e. stress at the REV scale). According to fracture mechanics principles, the average normal and shear displacement jumps for a single crack embedded in a linear isotropic elastic matrix can be expressed as follows [21, 46, 47]:

$$\begin{aligned}\langle[u_n]\rangle &= \frac{16}{3}\frac{1-\nu_0^2}{\pi E_0}\boldsymbol{\sigma} : (\overrightarrow{n}\otimes\overrightarrow{n})a \\ \langle[\overrightarrow{u_t}]\rangle &= \frac{32}{3}\frac{1-\nu_0^2}{(2-\nu_0)\pi E_0}[\boldsymbol{\sigma}\cdot\overrightarrow{n_i} - (\overrightarrow{n}\cdot\boldsymbol{\sigma}\cdot\overrightarrow{n})\overrightarrow{n}]a\end{aligned} \tag{2}$$

In which E_0 and ν_0 are the Young's modulus and Poisson's ratio of the matrix, respectively.

Correspondingly, the average volume fraction of the normal and shear displacement jumps for a single family of cracks are calculated as:

$$\beta = \frac{N}{|\Omega_r|}\langle[u_n]\rangle\pi a^2, \quad \overrightarrow{\gamma} = \frac{N}{|\Omega_r|}\langle[\overrightarrow{u_t}]\rangle\pi a^2 \tag{3}$$

The elastic free enthalpy of the cracked REV can be expressed as

$$G^* = \frac{1}{2}\boldsymbol{\sigma} : \boldsymbol{\epsilon} = \frac{1}{2}\boldsymbol{\sigma} : \mathbb{S}_0 : \boldsymbol{\sigma} + \frac{1}{2}\boldsymbol{\sigma} : [\beta\overrightarrow{n}\otimes\overrightarrow{n} + \frac{1}{2}(\overrightarrow{\gamma}\otimes\overrightarrow{n} + \overrightarrow{n}\otimes\overrightarrow{\gamma})] \tag{4}$$

A normal displacement jump can only be induced by a tensile force, i.e. for $\overrightarrow{n} \cdot \boldsymbol{\sigma} \cdot \overrightarrow{n} \geq 0$. The unilateral contact condition at crack faces can thus be expressed as:

$$[u_n] \geq 0, \quad \sigma_{nn} = \overrightarrow{n} \cdot \boldsymbol{\sigma} \cdot \overrightarrow{n} \geq 0, \quad [u_n]\sigma_{nn} = 0 \tag{5}$$

After combining all the equations above, the free enthalpy for the considered REV with a single set of N cracks is expressed as:

$$\begin{aligned} G^* =& \frac{1}{2}\boldsymbol{\sigma} : \mathbb{S}_0 : \boldsymbol{\sigma} + \frac{1}{2}c_0\rho(\overrightarrow{n} \cdot \boldsymbol{\sigma} \cdot \overrightarrow{n})\langle \overrightarrow{n} \cdot \boldsymbol{\sigma} \cdot \overrightarrow{n}\rangle^+ \\ &+ \frac{1}{2}c_1\rho[(\boldsymbol{\sigma} \cdot \boldsymbol{\sigma}) : (\overrightarrow{n} \otimes \overrightarrow{n}) - \boldsymbol{\sigma} : (\overrightarrow{n} \otimes \overrightarrow{n} \otimes \overrightarrow{n} \otimes \overrightarrow{n}) : \boldsymbol{\sigma}] \end{aligned} \tag{6}$$

In which we note $\langle x\rangle^+ = x, x \geq 0$, and $\langle x\rangle^+ = 0, x < 0$. The coefficient c_0 (respectively c_1) is defined as the normal (respectively shear) elastic compliance of the crack. $\rho(\overrightarrow{n})$ is the crack density, for the set of N cracks oriented in planes perpendicular to $\overrightarrow{n}$. We define:

$$c_0 = \frac{16}{3}\frac{1-\nu_0^2}{E_0}, \quad c_1 = \frac{32}{3}\frac{1-\nu_0^2}{(2-\nu_0)E_0}, \quad \rho = \frac{Na^3}{|\Omega_r|} \tag{7}$$

For several crack sets of different orientations, the Gibbs free energy of the REV is obtained by integrating G^* for a distribution of crack densities $\rho(\overrightarrow{n})$, over the unit sphere $S^2 = \{\overrightarrow{n}, |\overrightarrow{n}| = 1\}$, as follows:

$$\begin{aligned} G =& \frac{1}{2}\boldsymbol{\sigma} : \mathbb{S}_0 : \boldsymbol{\sigma} + \frac{1}{8\pi}\int_{S^2} \{c_0\,\rho(\overrightarrow{n})(\overrightarrow{n} \cdot \boldsymbol{\sigma} \cdot \overrightarrow{n})\langle \overrightarrow{n} \cdot \boldsymbol{\sigma} \cdot \overrightarrow{n}\rangle^+ \\ &+ c_1\,\rho(\overrightarrow{n})[(\boldsymbol{\sigma} \cdot \boldsymbol{\sigma}) : (\overrightarrow{n} \otimes \overrightarrow{n}) - \boldsymbol{\sigma} : (\overrightarrow{n} \otimes \overrightarrow{n} \otimes \overrightarrow{n} \otimes \overrightarrow{n}) : \boldsymbol{\sigma}]\}\mathrm{d}S \end{aligned} \tag{8}$$

At the scale of the REV, the second order crack density tensor $\boldsymbol{\rho}$ is defined in such a way that: $\rho(\overrightarrow{n}) = \overrightarrow{n} \cdot \boldsymbol{\rho} \cdot \overrightarrow{n}$. The second order damage tensor is defined as follows:

$$\boldsymbol{\Omega} = \frac{1}{4\pi}\int_{S^2} \rho(\overrightarrow{n})(\overrightarrow{n} \otimes \overrightarrow{n})\mathrm{d}S = \frac{1}{4\pi}\int_0^{2\pi}\int_0^{\pi} \rho(\overrightarrow{n})(\overrightarrow{n} \otimes \overrightarrow{n})sin\theta \mathrm{d}\phi\mathrm{d}\theta \tag{9}$$

It can be shown mathematically (see [48, 49] for details) that the crack density function $\rho(\overrightarrow{n})$ is related to the damage tensor as follows:

$$\rho(\overrightarrow{n}) = \frac{3}{2}(5\,\overrightarrow{n}\cdot\boldsymbol{\Omega}\cdot\overrightarrow{n} - \mathrm{Tr}\boldsymbol{\Omega}) \tag{10}$$

The free energy is the sum of the elastic deformation energy stored in the matrix and the elastic energy stored by displacement jumps across crack surfaces. Let us consider two particular cases: either all cracks are open ($\overrightarrow{n}\cdot\boldsymbol{\sigma}\cdot\overrightarrow{n} > 0$), or all cracks are closed. After introducing the relation 10 in the expression of Gibbs energy and integrating over the unit sphere (Eq.9), we obtain the macroscopic free enthalpy in terms of second order damage tensor $\boldsymbol{\Omega}$, as follows:

$$\begin{aligned} G(\boldsymbol{\sigma},\boldsymbol{\Omega}) =& \frac{1}{2}\boldsymbol{\sigma} : \mathbb{S}_0 : \boldsymbol{\sigma} + a_1\,\mathrm{Tr}\boldsymbol{\Omega}(\mathrm{Tr}\boldsymbol{\sigma})^2 + a_2\,\mathrm{Tr}(\boldsymbol{\sigma}\cdot\boldsymbol{\sigma}\cdot\boldsymbol{\Omega}) \\ &+ a_3\,\mathrm{Tr}\boldsymbol{\sigma}\,\mathrm{Tr}(\boldsymbol{\Omega}\cdot\boldsymbol{\sigma}) + a_4\,\mathrm{Tr}\boldsymbol{\Omega}\,\mathrm{Tr}(\boldsymbol{\sigma}\cdot\boldsymbol{\sigma}) \end{aligned} \tag{11}$$

The four coefficients a_1, a_2, a_3 and a_4 are given as

$$a_1 = \frac{-\mu}{140}c_1, \quad a_2 = \frac{7+2\mu}{14}c_1, \quad a_3 = \frac{\mu}{14}c_1, \quad a_4 = \frac{-\mu}{70}c_1 \tag{12}$$

With $\mu = -\nu_0$ for open cracks and $\mu = -2$ for closed cracks. Note that the expression of the free enthalpy obtained from micro-mechanical principles in Eq.11 is similar to that assumed in a number of purely phenomenological models, e.g. [11, 15]. The damage driving force (energy release rate), conjugated to the damage tensor, is defined as:

$$\boldsymbol{Y} = \frac{\partial G(\boldsymbol{\sigma},\boldsymbol{\Omega})}{\partial\boldsymbol{\Omega}} = a_1\,(\mathrm{Tr}\boldsymbol{\sigma})^2\,\boldsymbol{\delta} + a_2\,\boldsymbol{\sigma}\cdot\boldsymbol{\sigma} + a_3\,\mathrm{Tr}(\boldsymbol{\sigma})\boldsymbol{\sigma} + a_4\,\mathrm{Tr}(\boldsymbol{\sigma}\cdot\boldsymbol{\sigma})\boldsymbol{\delta} \tag{13}$$

The isosurfaces of the principal damage driving forces defined in Eq.13 are shown in Fig 1. For closed cracks, each principal energy release rate Y_i is

symmetric with respect to the surface σ_i. For open crack cracks, the iso-contours of each principal damage driving force Y_i are concentrical ellipses, in which the short axis of the ellipses coincides with the principal stress directions σ_i. Note that $\boldsymbol{Y}$ is always positive. Since the damage rate $\dot{\Omega}$ is non-negative at any circumstances, the dissipation is always positive, i.e. the second law of thermodynamics is satisfied:

$$\boldsymbol{Y} : \dot{\boldsymbol{\Omega}} \geq 0 \tag{14}$$

The stress/strain relation is obtained by thermodynamic conjugation:

$$\begin{aligned}\boldsymbol{\epsilon} = \frac{\partial G(\boldsymbol{\sigma}, \boldsymbol{\Omega})}{\partial \boldsymbol{\sigma}} =& \frac{1+\nu_0}{E_0}\boldsymbol{\sigma} - \frac{\nu_0}{E_0}(\mathrm{Tr}\boldsymbol{\sigma})\,\boldsymbol{\delta} + 2a_1(\mathrm{Tr}\boldsymbol{\Omega}\,\mathrm{Tr}\boldsymbol{\sigma})\,\boldsymbol{\delta} + a_2(\boldsymbol{\sigma}\cdot\boldsymbol{\Omega} + \boldsymbol{\Omega}\cdot\boldsymbol{\sigma}) \\ &+ a_3[\,\mathrm{Tr}(\boldsymbol{\sigma}\cdot\boldsymbol{\Omega})\,\boldsymbol{\delta} + (\mathrm{Tr}\boldsymbol{\sigma})\,\boldsymbol{\Omega}\,] + 2a_4(\mathrm{Tr}\boldsymbol{\Omega})\,\boldsymbol{\sigma}\end{aligned} \tag{15}$$

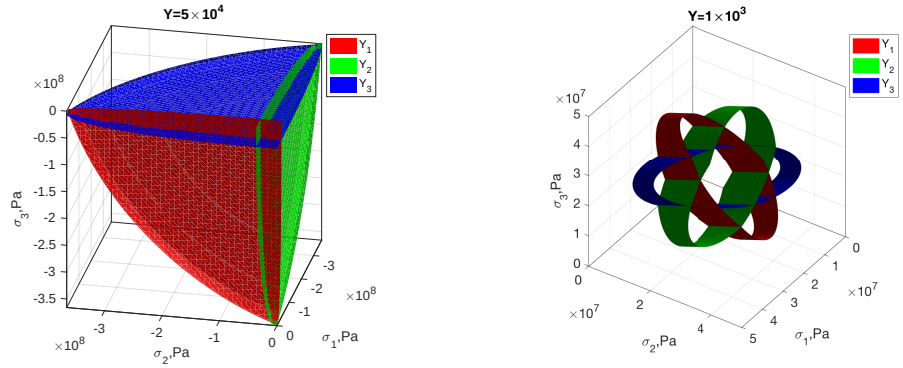

(a) Closed cracks

(b) Open cracks

Figure 1: Damage driving force isosurfaces in the space of principal stresses

2.2. Phenomenological damage criteria and evolution law

Due to the distinct behavior of brittle solids in tension (open cracks) and compression (closed cracks), we formulate two damage evolution laws and utilize the volumetric strain to distinguish tensile and compressive loading. Equivalent strains for tension ($\hat{\epsilon}_t$) and compression ($\hat{\epsilon}_c$) are defined as:

$$\begin{aligned} \hat{\epsilon}_t &= \sqrt{\sum_{I=1}^{3} \langle \epsilon_I \rangle^2}, \quad \text{if } \mathrm{Tr}\boldsymbol{\epsilon} > 0 \\ \hat{\epsilon}_c &= \sqrt{\sum_{I=1}^{3} \langle e_I \rangle^2}, \quad \text{if } \mathrm{Tr}\boldsymbol{\epsilon} \leq 0 \end{aligned} \tag{16}$$

In which ϵ_I are the principal strain components and e_I are the principal deviatoric strain components calculated as $e_I = \epsilon_I - \mathrm{Tr}\boldsymbol{\epsilon}/3$. We consider linear hardening/softening in the damage criteria:

$$\begin{aligned} f_t &= \hat{\epsilon}_t - (\kappa_t + \alpha_t \mathrm{Tr}\boldsymbol{\Omega}) \\ f_c &= \hat{\epsilon}_c + \eta \mathrm{Tr}\boldsymbol{\epsilon} - (\kappa_c + \alpha_c \mathrm{Tr}\boldsymbol{\Omega}) \end{aligned} \tag{17}$$

The volumetric strain in the expression of the compression damage criterion allows capturing the brittle-ductile transition that occurs upon increasing confining pressure. Fig.2 shows the damage surfaces in plane strain conditions, with two different values of damage, for the material parameters listed in Table 1.

Damage evolution laws in tension and compression are postulated so as to obtain damage patterns that conform to the observations made in [12], as follows:

$$\dot{\boldsymbol{\Omega}} = \dot{\lambda}_t \boldsymbol{D}_t = \dot{\lambda}_t \begin{bmatrix} \langle \epsilon_1 \rangle^2 / \hat{\epsilon}_t^2 & 0 & 0 \\ 0 & \langle \epsilon_2 \rangle^2 / \hat{\epsilon}_t^2 & 0 \\ 0 & 0 & \langle \epsilon_3 \rangle^2 / \hat{\epsilon}_t^2 \end{bmatrix}, \tag{18}$$

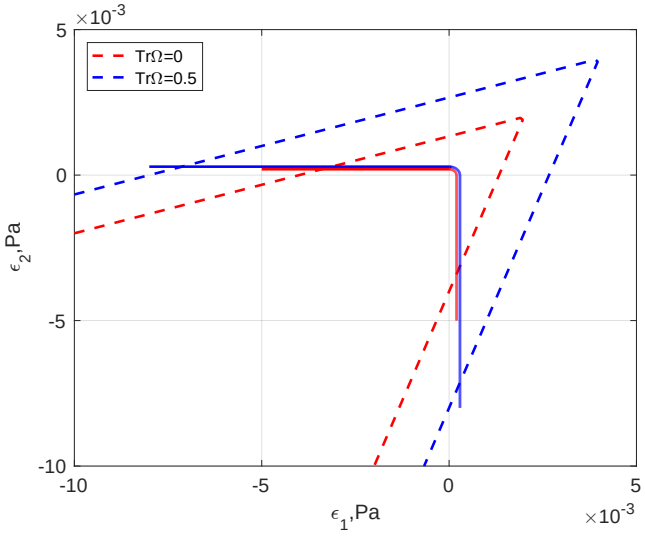

Figure 2: Damage surfaces at different damage levels in plane strain condition. Dashed lines represent compressive yield surfaces, solid lines represent tensile yield surfaces.

$$\dot{\boldsymbol{\Omega}} = \dot{\lambda}_c \boldsymbol{D}_c = \dot{\lambda}_c \begin{bmatrix} \langle e_1 \rangle^2 / \hat{\epsilon}_c^2 & 0 & 0 \\ 0 & \langle e_2 \rangle^2 / \hat{\epsilon}_c^2 & 0 \\ 0 & 0 & \langle e_3 \rangle^2 / \hat{\epsilon}_c^2 \end{bmatrix}. \tag{19}$$

In which the Lagrange multipliers $\dot{\lambda}_t$ and $\dot{\lambda}_c$ are determined from consistency conditions applied to the damage criteria (Eq.17). We can easily verify that a uniaxial tensile loading in direction 1 will result in cracks perpendicular to direction 1 because $\hat{\epsilon}_t = \epsilon_1 > 0$. A triaxial compression test with loading axis in direction 1 results in lateral damage (i.e. cracks perpendicular to directions 2 and 3) because $\hat{\epsilon}_c = \sqrt{2}e_2 = \sqrt{2}e_3 > 0$, even when all the strain components are negative.

Table 1: Material parameters used for ploting the yield surfaces in Fig.2 and for performing the Gauss point simulations in Section 2.3.

Elasticity		Tension		Compression		
E_0/GPa	ν_0	κ_t	α_t	κ_c	α_c	η
38	0.18	2.0×10^{-4}	1.8×10^{-4}	1.0×10^{-3}	2.0×10^{-3}	0.5

For compressive loadings, we have:

$$\begin{aligned} 0 =& \frac{\partial f_c}{\partial \hat{\epsilon}_c} \mathrm{d}\hat{\epsilon}_c + \frac{\partial f_c}{\partial \mathrm{Tr}\boldsymbol{\epsilon}} \mathrm{d}(\mathrm{Tr}\boldsymbol{\epsilon}) + \frac{\partial f_c}{\partial \boldsymbol{\Omega}} : \mathrm{d}\boldsymbol{\Omega} \\ =& \dot{\hat{\epsilon}}_c + \eta \boldsymbol{\delta} : \mathrm{d}\boldsymbol{\epsilon} - \alpha_c \boldsymbol{\delta} : \dot{\boldsymbol{\Omega}} \end{aligned} \tag{20}$$

By substituting the compressive flow rule (Eq.19) into Eq.20, we obtain the expression of the Lagrange multiplier as:

$$\dot{\lambda}_c = \frac{\dot{\hat{\epsilon}}_c + \eta \boldsymbol{\delta} : \mathrm{d}\boldsymbol{\epsilon}}{\alpha_c} \tag{21}$$

Note that by construction of the flow rule (Eq.19), we have $\alpha_c \boldsymbol{\delta} : \dot{\boldsymbol{\Omega}} = \alpha_c \dot{\lambda}_c$. In the same way, for tensile loading, we have

$$\dot{\lambda}_t = \dot{\hat{\epsilon}}_t / \alpha_t \tag{22}$$

2.3. Simulations at the material point

We implemented the proposed anisotropic model into ABAQUS Finite Element package, in a UMAT subroutine. We consider a cubic element, with 8 nodes and 8 Gauss points. Table 1 summarizes the material parameters employed. We first simulate a sequence of tensile loading, unloading, compressive loading (under zero confinement), and tensile reloading. The vertical displacement of the bottom 4 nodes is set to zero. Two orthogonal horizontal

displacements are also set to zero to prevent free body movements. Positive and negative displacements are applied to the top 4 nodes to simulate tensile and compressive loading stages. Since damage evolution laws are strain based, no iterative process is needed for strain controlled tests. Note that for stress-controlled tests, governing equations have to be solved iteratively, to ensure that boundary conditions are satisfied (e.g., confining pressure). Stress, strain and damage values are averaged over the 8 Gauss points.

Fig.3 shows the stress-strain curve and the evolution of damage during the uniaxial tension/compression test. Initially, the material is elastic (A-B). The damage component perpendicular to the tensile loading axis grows linearly after the yield point has been reached (B), and the stress/strain curve then exhibits softening (B-C). During unloading, the material responds elastically. But due to damage accumulation, the slope of the stress/strain curve is lower than initially, i.e. the material has a lower stiffness (C-D). Upon further compression (D-E), the material recovers its initial stiffness due to unilateral effects (i.e. crack closure), and responds elastically (i.e. no damage development). Then, upon reloading in tension, the stress/strain curve is first identical to that obtained during tension unloading (E-F-G). When the stress reaches the value it had at the end of the first tensile loading phase (G), a new yielding point is reached: the stress/strain curve then exhibits softening, and damage grows again (G-H). Note that here, crack density was defined from micro-mechanical principles, and can thus exceed unity.

Next, we simulate a triaxial compression test under various confining pressures. Fig.4 shows the stress-strain curve and damage component evolution obtained for a single cubic element with 8 Gauss points. The element

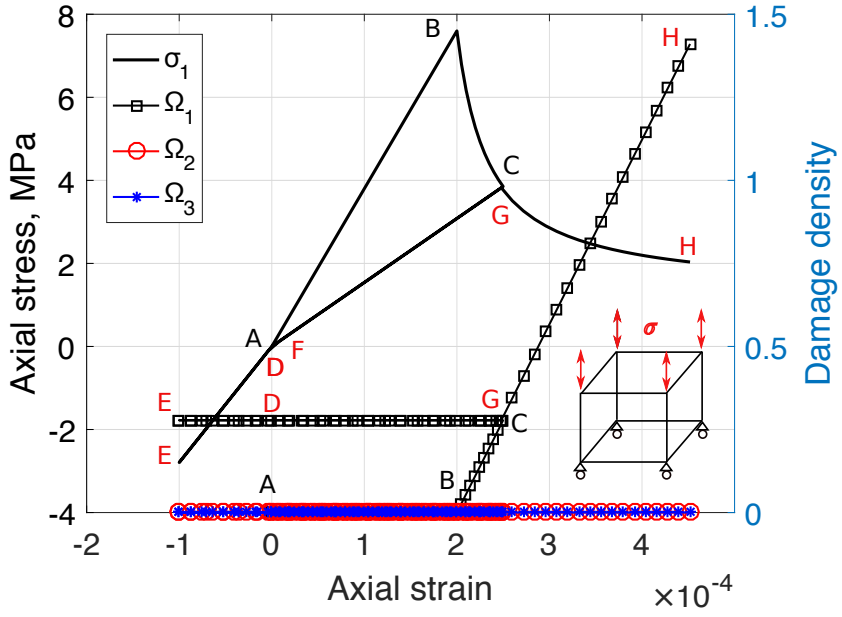

Figure 3: Simulation of a uniaxial tension-unloading-compression-tension loading sequence for a single element

geometry, material parameters and boundary conditions are the same as in the previous case, except that a confining pressure is applied on the lateral faces. A monotonic displacement-controlled compressive load is applied until damage components grow to some extent. For all confining pressures considered, triaxial compression resulted in lateral damage (i.e. crack planes containing the loading axis). The dependence of damage development on the confining pressure is captured by the model: in the simulations presented here, the yield stress is higher under 5 MPa confinement than under 0 MPa confinement. By examining the results of the uniaxial compression test in Fig.4 and of those of the uniaxial tension test in Fig.3, we note that tensile softening and compressive hardening are captured. In addition, a difference

of up to one order magnitude exists between tensile and compressive yield stresses, which is conform to experimental observations made on quasi-brittle materials.

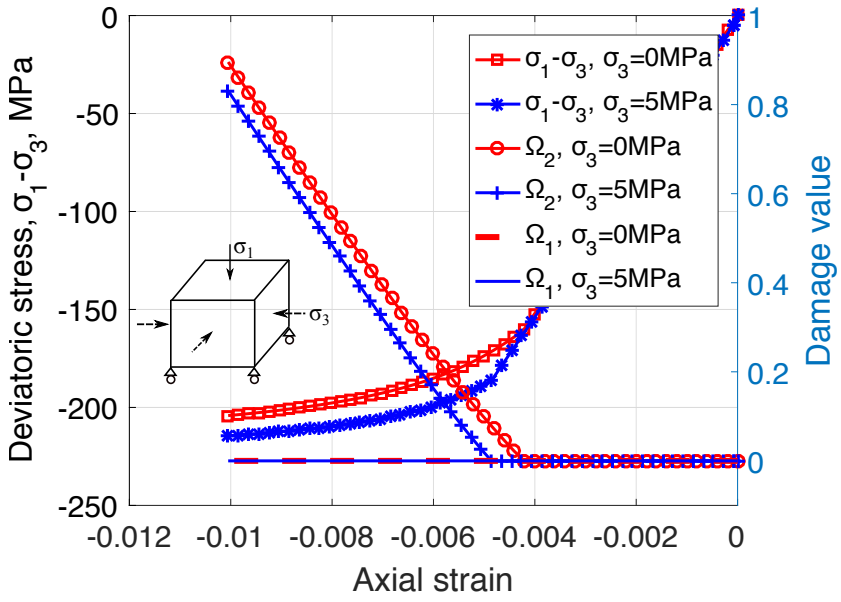

Figure 4: Simulation of triaxial compression tests under various confining pressures for a single element

3. Numerical implementation strategy for softening and snapback

3.1. Nonlocal regularization

As illustrated in Fig.3, the initiation and propagation of mode I cracks leads to strain softening, which makes the associated boundary value problem ill-posed. Numerically, the tensile failure path development is mesh dependent. The energy that needs to be released to create a unit surface of tensile fracture does not converge upon mesh refinement. This is inconsistent

with experimental observations, since the energy release rate is found to be material-specific [36]. To regularize the damage model formulated in section 2, we use an integration-based non-local technique [30]: the evolution of the damage variables at a material point does not only depend on the stress and strain at that point, but also on the field variables within an influence domain surrounding that point. The size of the nonlocal influence domain is controlled by a characteristic internal length, which is a material parameter usually equal to 2 to 3 times the maximum size of grains encountered in the polycrystal [1]. In order to account for the non-local nature of damage, we replaced the equivalent strains that control damage evolution (Eq.16) by their weighted average defined on an influence domain V, as follows:

$$\hat{\epsilon}_i^{nl}(\boldsymbol{x}) = \int_V \alpha(\boldsymbol{x}, \boldsymbol{\xi}) \hat{\epsilon}_i(\boldsymbol{\xi}) \mathbf{d}V(\boldsymbol{\xi}), \quad (i = t/c) \tag{23}$$

Where $\boldsymbol{x}$ is the position vector of the material point considered, and $\boldsymbol{\xi}$ is the position vector of points in the influence domain of $\boldsymbol{x}$. $\alpha(\boldsymbol{x}, \boldsymbol{\xi})$ is the nonlocal weight function, which decreases monotonically as the distance $r = \|\boldsymbol{x} - \boldsymbol{\xi}\|$ increases. Note that if field variables are uniform, the value of damage should be uniform. Hence the non-local value of the equivalent strains should be equal to the local value of equivalent strains in the uniform strain field. This implies that weight functions should satisfy the partition of unity:

$$\int_V \alpha(\boldsymbol{x}, \boldsymbol{\xi}) \mathbf{d}V(\boldsymbol{\xi}) = 1 \tag{24}$$

In order to satisfy the partition of unity, the weight functions usually take

the following general form:

$$\alpha(\boldsymbol{x},\boldsymbol{\xi}) = \frac{\alpha_0(\boldsymbol{x},\boldsymbol{\xi})}{\int_V \alpha_0(\boldsymbol{x},\boldsymbol{\xi})\mathbf{d}V(\boldsymbol{\xi})} = \frac{\alpha_0(\boldsymbol{x},\boldsymbol{\xi})}{V_r(\boldsymbol{x})} \tag{25}$$

Where $V_r(\boldsymbol{x})$ is the so-called characteristic volume. The exact form of the weight function $\alpha_0(\boldsymbol{x},\boldsymbol{\xi})$ depends on the material considered. The Gauss function (normal distribution) and the bell-shaped function are the most widely used weight functions for isotropic media. Herein, we adopt the bell-shaped function, expressed as:

$$\alpha_0(\boldsymbol{x},\boldsymbol{\xi}) = \left\langle 1 - \frac{\|\boldsymbol{x}-\boldsymbol{\xi}\|^2}{l_c^2} \right\rangle^2. \tag{26}$$

In which l_c is the characteristic length. The advantage of the bell-shaped function is that the nonlocal influence zone only depends on l_c: no cut-off is needed to ensure that the weight function is zero outside of the influence zone, as shown in Fig.5. In the Finite Element Method (FEM), nonlocal variables are calculated as the weighted average of local variables obtained iteratively at the Gauss points located in the influence zone [50]. For instance, the nonlocal equivalent strain for $i = t, c$ is expressed as:

$$\hat{\epsilon}_i^{nl}(\boldsymbol{x}) = \frac{\sum_{j=1}^{N_{GP}} \alpha_0(\|\boldsymbol{x}-\boldsymbol{\xi}_j\|)\hat{\epsilon}_i(\boldsymbol{\xi}_j)\Delta V_j}{\sum_{j=1}^{N_{GP}} \alpha_0(\|\boldsymbol{x}-\boldsymbol{\xi}_j\|)\Delta V_j} \tag{27}$$

Where N_{GP} the total number of Gauss points inside the influence zone of material point $\boldsymbol{x}$. ΔV_j is the integration volume associated with the $j-th$ Gauss point.

3.2. Arc length control

In addition to mesh dependency induced by softening in tension (mode I crack propagation), the global force-displacement response curve of a particular problem may exhibit one or multiple critical points. The classical

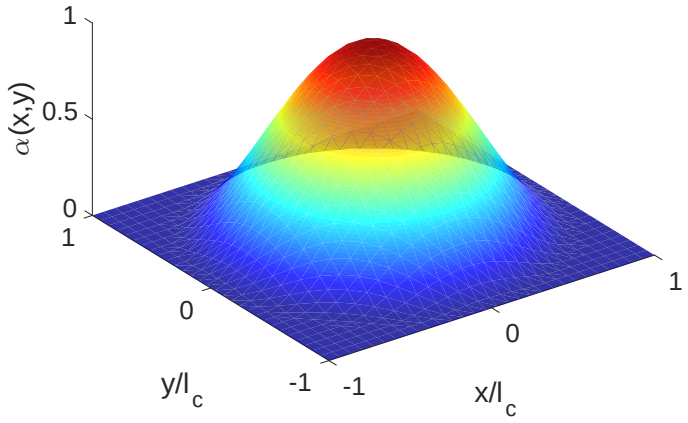

Figure 5: Bell-shaped nonlocal weight function with $l_c = 0.02$.

Newton-Raphson method is either load controlled or displacement controlled, and fails to predict snap back or snap through. To address this issue, we solve the balance equations by using the arc length control method [51], which allows passing all the critical points, as illustrated in Fig.6.

In the arc length control method, both the increment of load and the increment of displacement can be changed simultaneously, which involves an extra degree of freedom. In order to solve for all the unknowns, an additional balance equation is formulated in terms of the increments of load and displacement. This constraint ensures that converged solutions are indeed on the constitutive stress/strain curve. The most widely used arc length control constraint is expressed as [43]:

$$(\Delta \boldsymbol{u} + \delta \boldsymbol{u})^T \cdot (\Delta \boldsymbol{u} + \delta \boldsymbol{u}) + \psi^2 (\Delta \lambda + \delta \lambda)^2 (\boldsymbol{q}^T \cdot \boldsymbol{q}) = \Delta l^2 \tag{28}$$

where $\Delta \boldsymbol{u}$ is the increment of displacement ($\delta \boldsymbol{u}$ is the iterative correction),

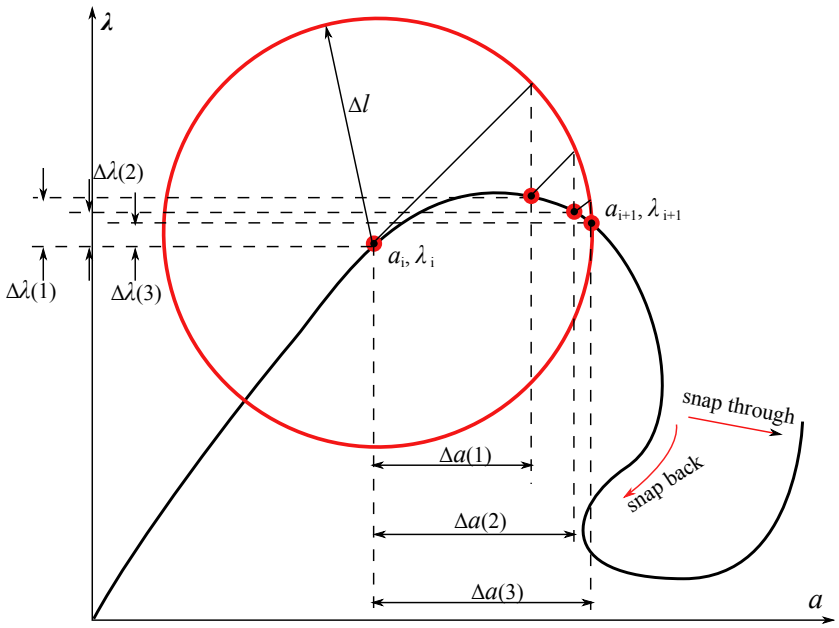

Figure 6: Principle of the arc-length control method. a denotes a normalized displacement, λ is the load scaling parameter. For a given increment, iterative values of a and λ are located on a circle of radius Δl.

$\boldsymbol{q}$ is the external load imposed and λ is a parameter controlling the intensity of the load increment. The scaling between load and displacement terms is controlled by the parameter ψ. When $\psi = 1$, the method is called spherical arc-length method: from Eq.28, equilibrium points are on the circle of radius Δl (Fig.6). Because the constraint equation involves all the degrees of freedom of the domain, the algorithm might still encounter convergence issues when localization occurs. Hence, we implement a local version of the arc length control method, based on the local normal plane method [44]: only the displacement of dominating elements, i.e. elements with non-zero damage at the beginning of each loading increment, are used to formulate the constraint

equation:

$$\sum_{e}[\nabla(\Delta \boldsymbol{u}_1^e)^T \nabla(\Delta \boldsymbol{u}_i^e)] = (\Delta l)^2 \quad (i = 1, 2, 3, ...) \tag{29}$$

Where e is the element number within the set of dominating elements. For an element with n nodes, $\nabla \boldsymbol{u}$ is the relative displacement vector, defined as follows:

$$\nabla(\boldsymbol{u}^e) = [u_1^e - u_n^e, u_2^e - u_1^e, u_3^e - u_2^e, ..., u_n^e - u_{n-1}^e] \tag{30}$$

We note $\Delta \boldsymbol{u}_i$ the incremental displacement vector at the i^{th} iteration, which is calculated as the sum of all the iterative displacements from iteration 1 to i:

$$\Delta \boldsymbol{u}_i = \Delta \boldsymbol{u}_{i-1} + \delta \boldsymbol{u}_i = \sum_{j=1}^{i} \delta \boldsymbol{u}_j \quad (i = 1, 2, 3, ...). \tag{31}$$

4. Non-Local Anisotropic Damage Model Calibration and Numerical Applications

4.1. Calibration algorithm

The local anisotropic damage model proposed in Section 2 depends on seven material parameters: E_0, ν_0, κ_c, α_c, η, κ_t, α_t. At least three independent tests are necessary to find these seven parameters: one tensile experiment, and two compressive stress/strain with different confining pressures. The response to a purely compressive stress path (respectively tensile stress path) does not depend on the tensile damage function parameters κ_t, α_t (respectively does not depend on the compressive damage parameters κ_c, α_c, η). In the following, we calibrate separately the tensile and compressive damage

parameters by using two independent sets of data: uniaxial tensile tests performed on concrete and triaxial compression tests performed on shale. Note that uniaxial tension tests can be simulated at the material point without any iterative procedure: since only the axial tensile strain contributes to damage growth, the stiffness matrix can be determined for each increment of axial strain, from which the values of total stress and strain can be calculated. For triaxial compression tests however, the implementation at the Gauss point is not as straightforward. For instance, if the simulation is controlled in displacement, deviatoric stress changes at each loading increment. When the damage threshold is reached, the material stiffness decreases, and the equilibrium equations require that the confining stress should decrease. Iterations are needed to calculate the stress and damage at equilibrium. In what follows, we control compression tests in stress, and we use a cutting plane algorithm, which is a type of return mapping algorithm [52].

The constitutive relationship in Eq.41 can be rewritten as

$$\boldsymbol{\varepsilon} = \mathbb{S}(\boldsymbol{\Omega}) : \boldsymbol{\sigma}, \tag{32}$$

where $\mathbb{S}$ is the compliance tensor, expressed as:

$$\begin{aligned}\mathbb{S}_{ijkl} = \frac{\partial \boldsymbol{\epsilon}}{\partial \boldsymbol{\sigma}} =& \frac{1+\nu_0}{2E_0}(\delta_{ik}\delta_{jl} + \delta_{il}\delta_{jk}) - \frac{\nu_0}{E_0}\delta_{ij}\delta_{kl} + 2a_1 \mathrm{Tr}\boldsymbol{\Omega}\, \delta_{ij}\delta_{kl} \\ &+ \frac{a_2}{2}(\delta_{ik}\Omega_{jl} + \delta_{il}\Omega_{jk} + \Omega_{ik}\delta_{jl} + \Omega_{il}\delta_{jk}) + a_3(\delta_{ij}\Omega_{kl} + \Omega_{ij}\delta_{kl}) \\ &+ a_4 \mathrm{Tr}\boldsymbol{\Omega}\, (\delta_{ik}\delta_{jl} + \delta_{il}\delta_{jk}).\end{aligned} \tag{33}$$

By differentiating the stress-strain relation in Eq.32, we get:

$$\mathrm{d}\boldsymbol{\varepsilon} = \mathbb{S}(\boldsymbol{\Omega}) : \mathrm{d}\boldsymbol{\sigma} + \boldsymbol{\sigma} : \partial_{\boldsymbol{\Omega}}\mathbb{S} : \mathrm{d}\boldsymbol{\Omega} \tag{34}$$

The yield function is linearized around values of the variables at increment $n+1$ and iteration i ($\boldsymbol{\epsilon}_{n+1}^{(i)}$, $\boldsymbol{\Omega}_{n+1}^{(i)}$), as follows:

$$f_{n+1}^{(i+1)} \approx f_{n+1}^{(i)} + \partial_{\boldsymbol{\epsilon}} f_{n+1}^{(i)} : [\boldsymbol{\epsilon}_{n+1}^{(i+1)} - \boldsymbol{\epsilon}_{n+1}^{(i)}] + \partial_{\boldsymbol{\Omega}} f_{n+1}^{(i)} : [\boldsymbol{\Omega}_{n+1}^{(i+1)} - \boldsymbol{\Omega}_{n+1}^{(i)}] \tag{35}$$

Assume that the test is controlled in stress $d\boldsymbol{\sigma}_{n+1}$. The trial strain $\boldsymbol{\epsilon}_{n+1}^{trial}$ is defined as $\boldsymbol{\epsilon}_{n+1}^{trial} = \boldsymbol{\epsilon}_{n+1}^{(0)} = \mathbb{S}(\boldsymbol{\Omega}_n) : d\boldsymbol{\sigma}_{n+1}$. If the yield criterion is exceeded, strains and damage are calculated iteratively as:

$$\begin{aligned} \boldsymbol{\epsilon}_{n+1}^{(i+1)} - \boldsymbol{\epsilon}_{n+1}^{(i)} &= \Delta\lambda_{n+1}^{(i)} [\boldsymbol{\sigma}_{n+1} : \partial_{\boldsymbol{\Omega}} \mathbb{S}_{n+1}^{(i)} : \boldsymbol{D}_n] \\ \boldsymbol{\Omega}_{n+1}^{(i+1)} - \boldsymbol{\Omega}_{n+1}^{(i)} &= \Delta\lambda_{n+1}^{(i)} \boldsymbol{D}_n \end{aligned} \tag{36}$$

In which $\Delta\lambda_{n+1}^{(i)}$ and $\boldsymbol{D}_n$ refer to compressive or tensile damage, depending on the stress path considered. After substituting Eq.36 in Eq.35, the Lagrange multiplier is calculated as:

$$\Delta\lambda_{n+1}^{(i)} = \frac{-f_{n+1}^{(i+1)}}{\partial_{\boldsymbol{\epsilon}} f_{n+1}^{(i)} : \boldsymbol{\sigma}_{n+1} : \partial_{\boldsymbol{\Omega}} \mathbb{S}_{n+1}^{(i)} : \boldsymbol{D}_n + \partial_{\boldsymbol{\Omega}} f_{n+1}^{(i)} : \boldsymbol{D}_n} \tag{37}$$

Table 2 explains the principle of the return mapping algorithm used for calculating strains and damage.

The calibration of the material parameters is actually a constrained optimization problem. The objective function, defined as the square of the distance between experimental results $\boldsymbol{y}$ and numerical predictions $f(\boldsymbol{x}, \boldsymbol{B})$, is expressed as:

$$R(\boldsymbol{B}) = \sum_{i=1}^{n} [y_i - f(x_i, \boldsymbol{B})]^2 \tag{38}$$

Where $\boldsymbol{x}$ stands for the vector of known input variables (e.g., strain/stress, depending on whether the load is controlled in force or displacement) and $\boldsymbol{B} = (E_0, \nu_0, \kappa_t, \alpha_t, \kappa_c, \alpha_c, \eta)$ is the vector of material parameters that need

Table 2: Cutting plane algorithm implemented in Matlab for the triaxial compression tests simulated at the Gauss point.

Step	Description
1	Initialize $\quad \boldsymbol{\epsilon}_{n+1}^{trial} = \boldsymbol{\epsilon}_n + \mathbb{S}(\boldsymbol{\Omega}) : \mathrm{d}\sigma_{n+1}$
	$\boldsymbol{\epsilon}_{n+1}^{(0)} = \boldsymbol{\epsilon}_{n+1}^{trial}$; $\quad \Omega_{n+1}^{(0)} = \Omega_n$; $\quad \lambda_{n+1}^{(0)} = 0$
2	Check the yield criteria
	IF: $f_{n+1}^{trial} \leq 0$ THEN: $\quad (\cdot)_{n+1} = (\cdot)_{n+1}^{tr}$, EXIT
	ELSE:
3	Compute increment of Lagrangian Multiplier
	$\Delta\lambda_{n+1}^{(i)} = \frac{-f_{n+1}^{(i+1)}}{\partial_{\boldsymbol{\epsilon}} f_{n+1}^{(i)} : \boldsymbol{\sigma}_{n+1} : \partial_{\boldsymbol{\Omega}} \mathbb{S}_{n+1}^{(i)} : \boldsymbol{D}_n + \partial_{\boldsymbol{\Omega}} f_{n+1}^{(i)} : \boldsymbol{D}_n}$
4	Update state variables and compute the new trial strain
	$\boldsymbol{\epsilon}_{n+1}^{(i+1)} = \boldsymbol{\epsilon}_{n+1}^{(i)} + \Delta\lambda_{n+1}^{(i)} [\boldsymbol{\sigma}_{n+1} : \partial_{\boldsymbol{\Omega}} \mathbb{S}_{n+1}^{(i)} : \boldsymbol{D}]$
	$\boldsymbol{\Omega}_{n+1}^{(i+1)} = \boldsymbol{\Omega}_{n+1}^{(i)} + \Delta\lambda_{n+1}^{(i)} \boldsymbol{D}$
	Goto 2.

to be calibrated. The lower and upper bounds of each parameter (found experimentally or by common sense) are used as constraints. We adopt the Interior Point Algorithm implemented in MATLAB with the function $fmincon$ to do the search iteration. We start with an initial guess $\boldsymbol{B}_0$. Then the gradient of the cost function $R(\boldsymbol{B})$ with respect to $\boldsymbol{B}$ is calculated. The steepest descendent direction is used to minimize the objective function as

$$\boldsymbol{B}_{n+1} = \boldsymbol{B}_n - \gamma_n \Delta f(\boldsymbol{x}, \boldsymbol{B}) \tag{39}$$

Where γ_n is the step size (which varies from one step to another). Since the objective function is not convex, the calibrated model parameters are not a global optimum of the constrained optimization problem. Therefore the final residual is calculated with different initial guesses, to ensure that the global optimum is found. For the details of the interior point algorithm, the reader is referred to [53, 54].

4.2. Compressive damage parameters and damage around a cavity

We first calibrate and validate the proposed model for compressive damage. Our reference data set is a series of triaxial compression test results obtained in ConocoPhillips rock mechanics laboratory [55]. The samples were all extracted from North Dakota Bakken shale at the same depth and and for the same lithology. Plugs were considered homogeneous. Here, the stress/strain curves obtained with confinements of 1000 psi (6.9 MPa) and 3000 psi (20.7 MPa) are used for calibration. Then the model is validated against the results obtained with a confinement of 2000 psi (13.8 MPa). Note that only the portion of the experimental data obtained before the peak of the stress/strain curve was used, because the proposed damage model is only

Table 3: Model parameters calibrated against triaxial compression tests reported in [55] for North Dakota Bakken shale

Elasticity		Yield Criteria		
E_0/GPa	ν_0	κ_c	α_c	η
35	0.254	1.0×10^{-3}	2.5×10^{-3}	0.6

valid for non-interacting cracks. Table 3 summarizes the values of the model parameters calibrated for shale subjected to compressive loading.

Fig.7 shows the results obtained after model calibration for confining pressures of $\sigma_3 = 6.9$, 13.8, 20.7 MPa. The numerical predictions match experimental results except for the lateral strain components. This discrepancy is mainly due to the basic constitutive assumption of the micromechanics model, in which only elastic crack sliding and opening are considered. In reality, shale is not purely brittle: plasticity occurs due to clay activity, inelastic pore collapse and geometric incompatibilities at crack faces. Despite these discrepancies in the lateral deformation components, the model captures the nonlinear behavior of shale under compression, with different responses at different confining pressures. This is because the compressive yield criterion depends on the volumetric strain (Tr$\boldsymbol{\epsilon}$). The evolution of damage components (or crack density components) follows that of the initial compressive yield stress $\sigma_1 - \sigma_3$, which increases linearly with the confining pressure σ_3 (see Fig.7(b)). Note that only lateral damage components grow during the triaxial compression test, which was expected. Overall, the micromechanics based damage model captures the behavior of quasi-brittle materials when tangential displacement jumps occur at closed micro-crack faces.

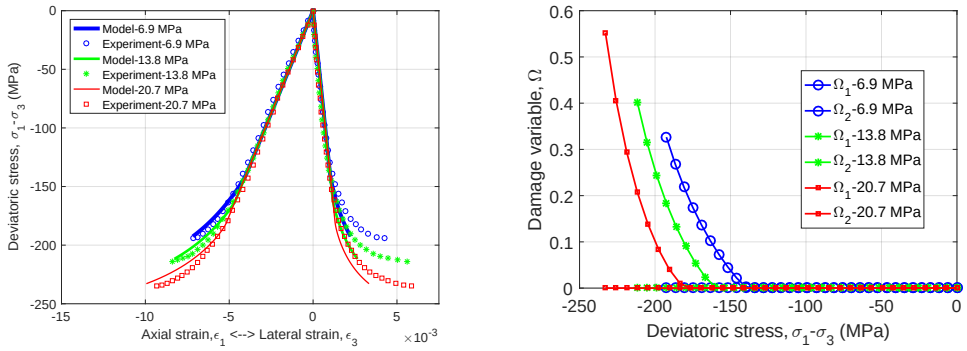

(a) (b)

Figure 7: Calibration and validation of the proposed model against triaxial compression tests performed on Bakken Shale. (a) Stress/strain curves (calibration based on data obtained at 6.9 MPa and 20.7 MPa confinement, and verification against tests performed under confining stress of 13.8 MPa). (b) Evolution of the principal values of damage during the tests.

We now simulate the initiation and propagation of cracks around a circular cavity with the model parameters calibrated in compression (Table 3), with a pseudo 3D model. The simulated domain and boundary conditions are shown in Fig.8. We applied an initial confining pressure ($\sigma_x = \sigma_y = \sigma_p$ =50 MPa) and simulated the following stress paths (Table 4): in case 1, we simulated a depressurization $\Delta\sigma_p = -50$MPa at the cavity wall followed by a vertical far field stress $\Delta\sigma_y = 50$MPa; in case 2, we simulated a vertical far field stress $\Delta\sigma_y = 50$MPa followed by a depressurization $\Delta\sigma_p = -50$MPa at the cavity wall; in case 3, we applied a vertical far field stress $\Delta\sigma_y = 50$MPa followed by a pressurization $\Delta\sigma_p = 100$MPa at the wall. In all cases, we set the displacements to zero along the z-axis to ensure plane strain conditions. Note that in all simulations, the domain is in a compressive state of stress,

Table 4: Simulation plan for different stress paths. Note the unit is in MPa.

Case	Step 0			Step 1		Step 2	
	σ_x	σ_y	σ_p	$\Delta\sigma_y$	$\Delta\sigma_p$	$\Delta\sigma_y$	$\Delta\sigma_p$
Case 1	50	50	50	0	-50	50	0
Case 2	50	50	50	50	0	0	-50
Case 3	50	50	50	50	0	0	100

so only hardening occurs (no softening). Since no mesh dependency is expected, we used an Abaqus UMAT subroutine to carry out the simulations. The mesh was made of more than 30,000 linear hexahedral elements.

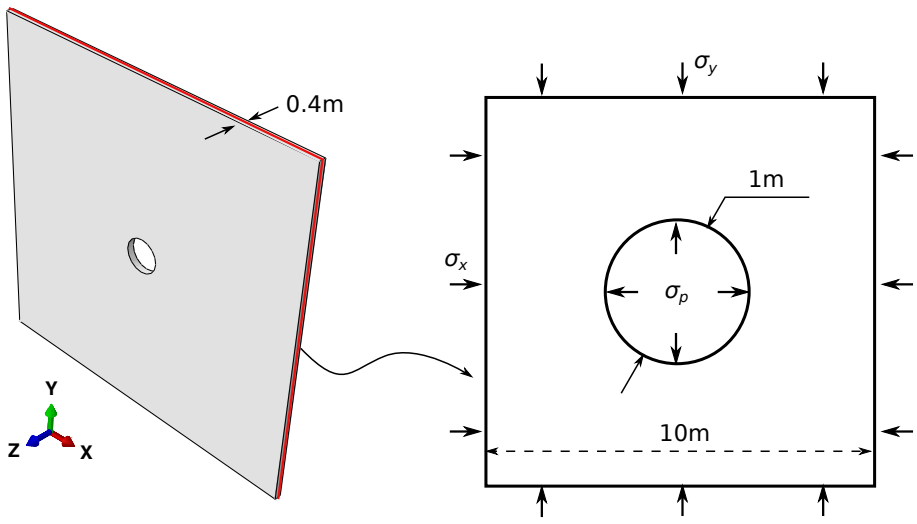

Figure 8: Geometry and boundary conditions for the cavity problem.

Fig.9 shows the final distributions of vertical (respectively horizontal) crack density Ω_x (respectively Ω_y) for the three stress paths. The maximum horizontal and vertical crack densities are higher in case 1 than in case

2, although the stress state is the same. Results thus show that the proposed model captures the dependence of damage development to the loading history. In both cases 1 and 2, significant vertical cracks (parallel to the maximum stress direction) develop at the two sides of the cavity. Horizontal cracks develop between the two vertical crack - damage zones. These damage distributions are consistent with the spalling zones observed in real engineering cases [45]. By contrast, in case 3, the main damage zones are located at the crown and bottom of the cavity, due to high pressure applied the cavity wall. In these two zones, the horozontal compressive stress is negligible compared to the vertical compressive stress, like in the laboratory splitting test. The continuous application of pressure at the cavity wall would result in two macro fractures initiated at the crown and bottom and propagating perpendicular to the main far field stress, like during hydraulic fracturing.

We define the elastic energy density (induced by purely elastic strain) and the elastic energy density due to crack opening and sliding as follows:

$$\begin{aligned} e_E &= \int_0^t \boldsymbol{\sigma} : \dot{\boldsymbol{\varepsilon}}^{el} \mathrm{d}\tau \\ e_\Omega &= \int_0^t \boldsymbol{\sigma} : \dot{\boldsymbol{\varepsilon}}^{ed} \mathrm{d}\tau \end{aligned} \tag{40}$$

Where

$$\begin{aligned} \boldsymbol{\epsilon}^{el} =& \frac{1+\nu_0}{E_0}\boldsymbol{\sigma} - \frac{\nu_0}{E_0}(\mathrm{Tr}\boldsymbol{\sigma})\,\boldsymbol{\delta} \\ \boldsymbol{\epsilon}^{ed} =& 2a_1(\mathrm{Tr}\boldsymbol{\Omega}\,\mathrm{Tr}\boldsymbol{\sigma})\,\boldsymbol{\delta} + a_2(\boldsymbol{\sigma}\cdot\boldsymbol{\Omega} + \boldsymbol{\Omega}\cdot\boldsymbol{\sigma}) \\ &+ a_3[\,\mathrm{Tr}(\boldsymbol{\sigma}\cdot\boldsymbol{\Omega})\,\boldsymbol{\delta} + (\mathrm{Tr}\boldsymbol{\sigma})\,\boldsymbol{\Omega}\,] + 2a_4(\mathrm{Tr}\boldsymbol{\Omega})\,\boldsymbol{\sigma} \end{aligned} \tag{41}$$

Fig. 10 shows the strain energy density distributions for case 1 (depressurization) and case 3 (pressurization). Note that case 2 is not represented, because

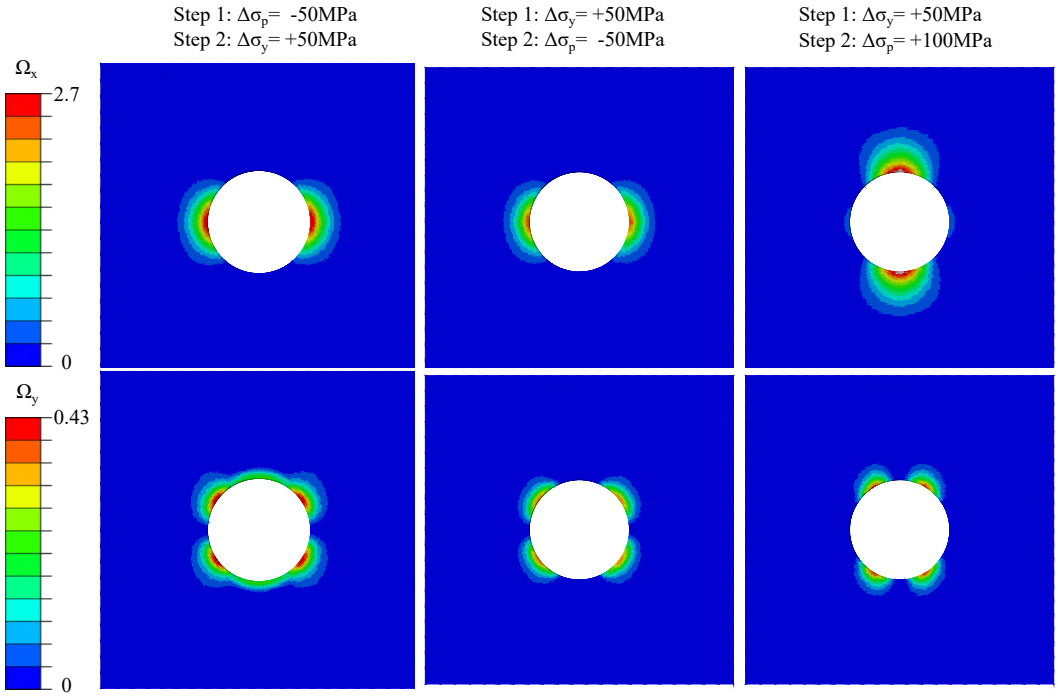

Figure 9: Distribution of Ω_x (vertical crack density) and Ω_y (horizontal crack density) in the three cavity cases. All cases encompass a fist loading stage of pressurization $\sigma_x = \sigma_y = \sigma_p$ =50 MPa. Note: the damage density can exceed 1 for the proposed model.

it exhibited similar results as case 1. More variability in the spatial distribution of the elastic energy density e_E is observed during depressurization (case 1) than pressurization (case 3). As expected, the spatial distribution of the damage induced elastic energy density e_Ω (due to crack opening) is similar to that of damage (Fig.9). In conclusion, the proposed damage model can predict complex compressive damage zones and can serve as a basis to couple REV-scale damage development and macro-fracture propagation in geophysical and geotechnical problems.

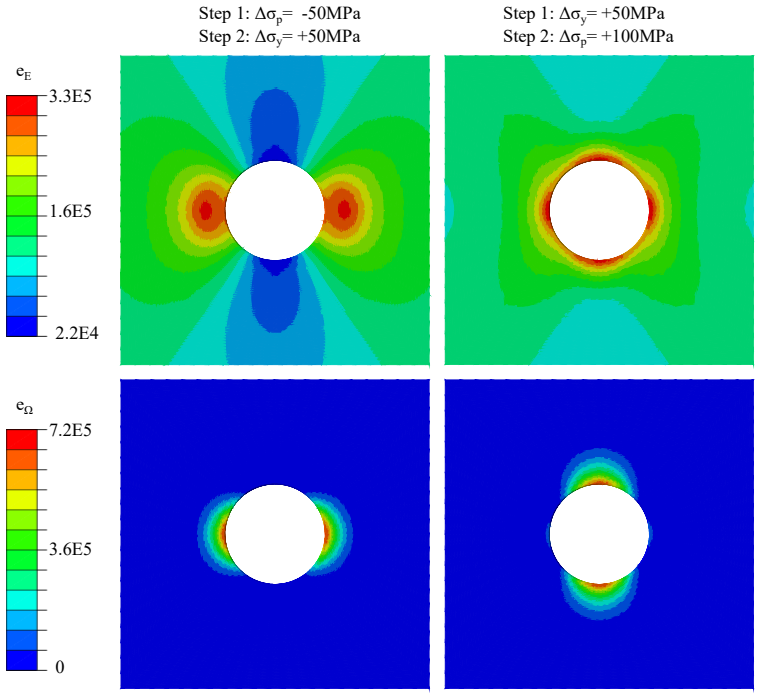

Figure 10: Distributions of elastic strain energy density (e_E) and damage induced elastic strain energy density (e_Ω) in cases 1 and 3 in Table 4.

4.3. Tensile damage parameters and three-point bending test simulation

We now calibrate the tensile damage model by using the algorithm described in Section 4.1. Note that if a direct tension test or a Brazilian test is conducted, tensile failure manifests in the form of a highly localized fracture and the load-displacement curve cannot be transformed into a stress/strain curve. Therefore, the reference data set was obtained by using a special apparatus "pour identifier l'endommagement diffus (PIED)" during uniaxial tension tests performed on concrete [1]. The PIED apparatus constrains the deformation in such a way that micro-cracks are uniformly distributed within the specimen. Such distributions can be predicted by the damage model pro-

Table 5: Model parameters calibrated against uniaxial tension tests reported in [1] for concrete.

Elasticity		Yield Criteria	
E_0/GPa	ν_0	κ_t	α_t
16.16	0.25	3.68×10^{-4}	4.74×10^{-4}

posed in Section 2. Calibration results are summarized in Table 5 and shown in Fig.11. Fig.11(b) shows that cracks develop in planes perpendicular to the loading direction (i.e. damage component parallel to the loading direction). Overall, the two tensile damage parameters κ_t and α_t can be calibrated to capture the beginning of tensile softening, but the model predictions do not match experimental data at the later stages of the tensile tests. This limitation is attributed to the fact that the proposed model does not account for micro-crack interaction or coalescence, and therefore, total tensile failure in the form of a macroscopic fracture cannot be predicted.

In the following, we simulate a three-point bending test with the damage model proposed in Section 2 calibrated for concrete. Cracks propagate in mixed mode, with tensile softening. Fig.12 shows the geometry and boundary conditions. To avoid localization issues, we implemented the non-local enrichment technique proposed in Section 3.1 in the Objective Oriented Finite Element Method (OOFEM) code [56] and we used the local version of the normal plane arc length control algorithm presented in Section 3.2 in plane strain conditions. Fig.13 shows the distribution of damage computed with two mesh refinements, with and without the nonlocal enhancement described in Section 3.1. In the nonlocal computations, the characteristic in-

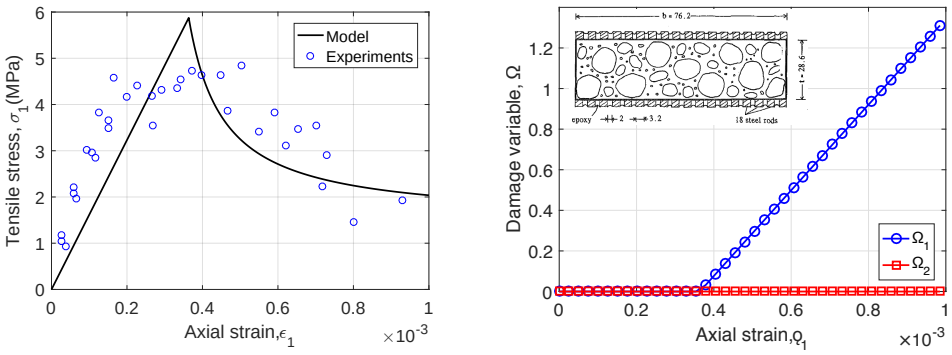

(a) Calibration of the proposed model with stress/strain curves

(b) Prediction of damage with the proposed model

Figure 11: Calibration of the damage model against uniaxial tension experimental data obtained for concrete [1] for open crack propagation.

ternal length l_c was set to 0.01m (which corresponds to 3-6 times the size of the aggregates in concrete). Note that damage components were normalized for the sake of comparison. All simulations yield mode I vertical cracks (horizontal damage), which is conform to the expectations. The results obtained with the local damage model are mesh dependent (see Fig.13(a) and 13(c)). If the mesh had been refined further, the failure process zone would have been reduced to a very small domain, with an energy dissipation close to zero. Non-local enhancement avoids mesh dependency at the initial stage of crack development: the width of the process zone is the same for both mesh refinements (marked with a rectangle in Fig.13(b) and 13(d)). However, the shape of the damage process zone is still mesh dependent. This is because the absence of micro-crack interaction in the proposed model makes it impossible to capture the total tensile stress relaxation after the peak tensile stress has been reached. To overcome this issue, not only non-local enhance-

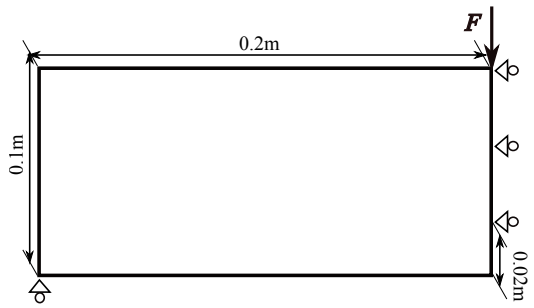

Figure 12: Geometry and boundary conditions of the (symmetrical) three point bending test simulated with the proposed damage model.

ment but also coupling between continuum damage mechanics and discrete fracture mechanics is needed. In future work, we plan to couple our non-local damage model with the XFEM, in order to switch from diffuse micro-crack propagation to localized macroscopic fracture propagation when coalescence initiates. A preliminary model coupling continuum damage mechanics and a Cohesive Zone Model (CZM) was proposed by the authors for mode II fracture propagation, with no softening [57].

5. Conclusion

A nonlocal micromechanics based anisotropic damage model is formulated for brittle geomaterials. A dilute homogenization scheme is adopted for calculating the deformation energy of the REV, which is attributed to the elastic deformation of the matrix, and to the displacement jumps at open and closed micro-crack faces. Gibbs free energy is obtained by integrating the energy potentials of the different sets of micro-cracks on the unit sphere. An explicit expression of the free energy of the REV is provided when all

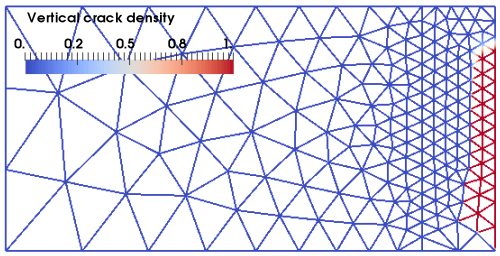

(a) Coarse mesh without nonlocal enhancement

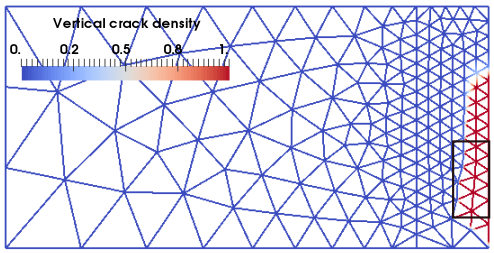

(b) Coarse mesh with nonlocal enhancement

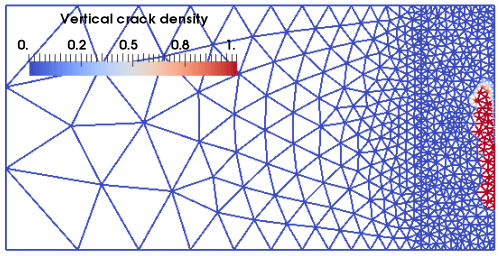

(c) Fine mesh without nonlocal enhancement

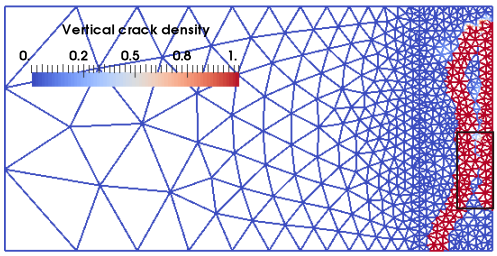

(d) Fine mesh with nonlocal enhancement

Figure 13: Horizontal damage component (i.e. vertical crack density) obtained by simulating a three-point bending test with the micro-mechanics based damage model, without and with non-local enhancement, for various mesh densities.

micro-cracks are open and when all micro-cracks are closed. Tensile (respectively compression) damage criteria depend on equivalent strains defined in terms of positive principal strains (respectively deviatoric) strains. Damage evolution laws are obtained from consistency conditions and from postulates on damage potentials. The model is enriched by non-local equivalent strains, calculated as the weighted average of equivalent strains on an influence zone of material-specific characteristic size.

We calibrate the non-local damage parameters against published experi-

mental data for concrete and shale. We employ the arc-length control method to solve boundary-value problems with the finite element package OOFEM: the algorithm allows capturing softening, snap back and snap through behaviors. The model can be used to predict the compression damage zone around a cavity under biaxial far field stress conditions: high crack densities in planes perpendicular to the maximum stress direction are obtained at the sidewall or at the crown, depending on the vertical to horizontal stress ratio. The simulation of a three-point bending test with the proposed non-local model shows that no mesh dependency is noted during softening, as long as micro-cracks do not interact.

The expressions of the energy potentials at the foundation of the proposed anisotropic damage model derive from micro-mechanics, which confers some physical meaning to the constitutive parameters. Single element simulations of uniaxial tension-compression cycles and triaxial compression tests demonstrate that the proposed model captures the nonlinear damaged stress/strain behavior, damage induced stiffness anisotropy, loading path dependent strain softening/hardening, unilateral effects due to crack closure and the brittle-ductile transition, which depends on the confining pressure. Non-local enrichement avoids mesh dependency at the beginning of tensile softening, and the implementation of an algorithm such as the arc length control method is ensures convergency when the stress/strain response exhibits several critical points. Coupling with a Cohesive Zone Model is necessary to predict the advancement of a macroscopic fracture tip as a result of micro-crack initiation, propagation and coalescence.

Acknowledgements

Financial support for this research was provided by the U.S. National Science Foundation (grants 1552368 and 1449501).

References

[1] Z. P. Bazant, G. Pijaudier-Cabot, Measurement of characteristic length of nonlocal continuum, Journal of Engineering Mechanics 115 (4) (1989) 755–767.

[2] D. Krajcinovic, M. Basista, D. Sumarac, Micromechanically inspired phenomenological damage model, Journal of Applied Mechanics 58 (2) (1991) 305–310.

[3] A.-S. Chiarelli, J.-F. Shao, N. Hoteit, Modeling of elastoplastic damage behavior of a claystone, International Journal of Plasticity 19 (1) (2003) 23–45.

[4] D. Candappa, J. Sanjayan, S. Setunge, Complete triaxial stress-strain curves of high-strength concrete, Journal of Materials in Civil Engineering 13 (3) (2001) 209–215.

[5] S. Yuan, J. Harrison, A review of the state of the art in modelling progressive mechanical breakdown and associated fluid flow in intact heterogeneous rocks, International Journal of Rock Mechanics and Mining Sciences 43 (7) (2006) 1001–1022.

[6] S. Murakami, Mechanical modeling of material damage, Journal of Applied Mechanics 55 (2) (1988) 280–286.

[7] J. Mazars, G. Pijaudier-Cabot, Continuum damage theory-application to concrete, Journal of Engineering Mechanics 115 (2) (1989) 345–365.

[8] D. Halm, A. Dragon, A model of anisotropic damage by mesocrack growth; unilateral effect, International Journal of Damage Mechanics 5 (4) (1996) 384–402.

[9] J. Simo, J. Ju, Strain-and stress-based continuum damage models—i. formulation, International journal of solids and structures 23 (7) (1987) 821–840.

[10] J. Ju, On energy-based coupled elastoplastic damage theories: constitutive modeling and computational aspects, International Journal of Solids and structures 25 (7) (1989) 803–833.

[11] M. Kachanov, Continuum model of medium with cracks, Journal of the engineering mechanics division 106 (5) (1980) 1039–1051.

[12] A. Dragon, D. Halm, T. Désoyer, Anisotropic damage in quasi-brittle solids: modelling, computational issues and applications, Computer methods in applied mechanics and engineering 183 (3) (2000) 331–352.

[13] H. Xu, C. Arson, Anisotropic damage models for geomaterials: theoretical and numerical challenges, International Journal of Computational Methods 11 (02) (2014) 1342007.

[14] I. Collins, G. Houlsby, Application of thermomechanical principles to the modelling of geotechnical materials, in: Proceedings of the Royal Society of London A: Mathematical, Physical and Engineering Sciences, Vol. 453, The Royal Society, 1997, pp. 1975–2001.

[15] K. Hayakawa, S. Murakami, Thermodynamical modeling of elastic-plastic damage and experimental validation of damage potential, International Journal of damage mechanics 6 (4) (1997) 333–363.

[16] D. Krajcinovic, D. Fanella, A micromechanical damage model for concrete, Engineering Fracture Mechanics 25 (5) (1986) 585–596.

[17] L. Gambarotta, S. Lagomarsino, A microcrack damage model for brittle materials, International Journal of Solids and Structures 30 (2) (1993) 177–198.

[18] V. Pensée, D. Kondo, L. Dormieux, Micromechanical analysis of anisotropic damage in brittle materials, Journal of Engineering Mechanics 128 (8) (2002) 889–897.

[19] V. Pensee, D. Kondo, Micromechanics of anisotropic brittle damage: comparative analysis between a stress based and a strain based formulation, Mechanics of materials 35 (8) (2003) 747–761.

[20] G. Swoboda, Q. Yang, An energy-based damage model of geomaterials—i. formulation and numerical results, International journal of solids and structures 36 (12) (1999) 1719–1734.

[21] B. Budiansky, R. J. O'connell, Elastic moduli of a cracked solid, International Journal of Solids and Structures 12 (2) (1976) 81–97.

[22] X. Lee, J. Ju, Micromechanical damage models for brittle solids. part ii: compressive loadings, Journal of Engineering Mechanics 117 (7) (1991) 1515–1536.

[23] J. Ju, X. Lee, Micromechanical damage models for brittle solids. part i: tensile loadings, Journal of Engineering Mechanics 117 (7) (1991) 1495–1514.

[24] T. Mori, K. Tanaka, Average stress in matrix and average elastic energy of materials with misfitting inclusions, Acta metallurgica 21 (5) (1973) 571–574.

[25] Q. Zhu, D. Kondo, J. Shao, Micromechanical analysis of coupling between anisotropic damage and friction in quasi brittle materials: role of the homogenization scheme, International Journal of Solids and Structures 45 (5) (2008) 1385–1405.

[26] Q. Zhu, D. Kondo, J.-F. Shao, Homogenization-based analysis of anisotropic damage in brittle materials with unilateral effect and interactions between microcracks, International Journal for Numerical and Analytical Methods in Geomechanics 33 (6) (2009) 749–772.

[27] W. Jin, C. Arson, Discrete equivalent wing crack based damage model for brittle solids, International Journal of Solids and Structures 110-111 (2017) 279–293.

[28] B. Paliwal, K. Ramesh, An interacting micro-crack damage model for failure of brittle materials under compression, Journal of the Mechanics and Physics of Solids 56 (3) (2008) 896–923.

[29] W. Jin, C. Arson, Micromechanics based discrete damage model with multiple non-smooth yield surfaces: theoretical formulation, numerical

implementation and engineering applications, in: International Journal of Damage Mechanics, 2017.

[30] G. Pijaudier-Cabot, Z. P. Bazant, Nonlocal damage theory, Journal of Engineering Mechanics 113 (10) (1987) 1512–1533.

[31] Z. P. Bazant, G. Pijaudier-Cabot, Nonlocal continuum damage, localization instability and convergence, Journal of Applied Mechanics 55 (2) (1988) 287–293.

[32] R. De Borst, J. Pamin, R. Peerlings, L. Sluys, On gradient-enhanced damage and plasticity models for failure in quasi-brittle and frictional materials, Computational Mechanics 17 (1-2) (1995) 130–141.

[33] R. Peerlings, R. De Borst, J. De Vree, Gradient enhanced damage for quasi-brittle materials, International Journal for numerical methods in engineering 39 (De Vree, JHP) (1996) 3391–3403.

[34] R. Peerlings, R. De Borst, W. Brekelmans, J. De Vree, I. Spee, Some observations on localisation in non-local and gradient damage models, EUROPEAN JOURNAL OF MECHANICS SERIES A SOLIDS 15 (1996) 937–954.

[35] R. Peerlings, R. De Borst, W. Brekelmans, M. Geers, Gradient-enhanced damage modelling of concrete fracture, Mechanics of Cohesive-frictional Materials 3 (4) (1998) 323–342.

[36] M. Jirasek, Nonlocal models for damage and fracture: comparison of approaches, International Journal of Solids and Structures 35 (31) (1998) 4133–4145.

[37] C. Comi, S. Mariani, U. Perego, From localized damage to discrete cohesive crack propagation in nonlocal continua, in: Proceedings of the Fifth World Congress on Computational Mechanics (WCCM V), Vienna University of Technology, 2002.

[38] R. Desmorat, F. Gatuingt, F. Ragueneau, Nonlocal anisotropic damage model and related computational aspects for quasi-brittle materials, Engineering Fracture Mechanics 74 (10) (2007) 1539–1560.

[39] R. Duddu, H. Waisman, A nonlocal continuum damage mechanics approach to simulation of creep fracture in ice sheets, Computational Mechanics 51 (6) (2013) 961–974.

[40] W. He, Y.-F. Wu, Y. Xu, T.-T. Fu, A thermodynamically consistent nonlocal damage model for concrete materials with unilateral effects, Computer Methods in Applied Mechanics and Engineering 297 (2015) 371–391.

[41] R. Peerlings, M. Geers, R. De Borst, W. Brekelmans, A critical comparison of nonlocal and gradient-enhanced softening continua, International Journal of solids and Structures 38 (44) (2001) 7723–7746.

[42] M. Criesfield, Non linear finite element analysis of solids and structures, vol. 1 (1991).

[43] M. A. Crisfield, A fast incremental/iterative solution procedure that handles “snap-through”, Computers & Structures 13 (1) (1981) 55–62.

[44] I. May, Y. Duan, A local arc-length procedure for strain softening, Computers & structures 64 (1) (1997) 297–303.

[45] J. Shao, D. Hoxha, M. Bart, F. Homand, G. Duveau, M. Souley, N. Hoteit, Modelling of induced anisotropic damage in granites, International Journal of Rock Mechanics and Mining Sciences 36 (8) (1999) 1001–1012.

[46] M. Kachanov, Effective elastic properties of cracked solids: critical review of some basic concepts, Applied Mechanics Reviews 45 (8) (1992) 304–335.

[47] M. L. Kachanov, B. Shafiro, I. Tsukrov, Handbook of elasticity solutions, Springer Science & Business Media, 2013.

[48] V. Lubarda, D. Krajcinovic, Damage tensors and the crack density distribution, International Journal of Solids and Structures 30 (20) (1993) 2859–2877.

[49] Q. Yang, W. Zhou, G. Swoboda, Micromechanical identification of anisotropic damage evolution laws, International journal of fracture 98 (1) (1999) 55–76.

[50] J. De Vree, W. Brekelmans, M. Van Gils, Comparison of nonlocal approaches in continuum damage mechanics, Computers & Structures 55 (4) (1995) 581–588.

[51] E. Riks, An incremental approach to the solution of snapping and buckling problems, International Journal of Solids and Structures 15 (7) (1979) 529–551.

[52] J. Simo, T. J. Hughes, Computational inelasticity, volume 7 of interdisciplinary applied mathematics (1998).

[53] R. H. Byrd, J. C. Gilbert, J. Nocedal, A trust region method based on interior point techniques for nonlinear programming, Mathematical Programming 89 (1) (2000) 149–185.

[54] R. A. Waltz, J. L. Morales, J. Nocedal, D. Orban, An interior algorithm for nonlinear optimization that combines line search and trust region steps, Mathematical Programming 107 (3) (2006) 391–408.

[55] D. Amendt, S. Busetti, Q. Wenning, et al., Mechanical characterization in unconventional reservoirs: A facies-based methodology, Petrophysics 54 (05) (2013) 457–464.

[56] B. Patzák, Oofem—an object-oriented simulation tool for advanced modeling of materials and structures, Acta Polytechnica 52 (6).

[57] W. Jin, H. Xu, C. Arson, S. Busetti, Computational model coupling mode ii discrete fracture propagation with continuum damage zone evolution, International Journal for Numerical and Analytical Methods in Geomechanics 41 (2) (2017) 223–250.